Wafer-scale Graphene Synthesized by Chemical Vapor Deposition at Ambient Pressure

Helin Cao[1,2,#], Qingkai Yu[3,#,], Luis A. Jauregui[2,5], Jifa Tian[1,2], Wei Wu[3], Zhihong Liu[3], Romaneh Jalilian[1,2], Daniel K. Benjamin[4], Zhigang Jiang[4], Jiming Bao[3], Steven S.S. Pei[3] and Yong P. Chen[1,2,5,*]*

[1] Department of Physics, Purdue University, West Lafayette, IN 47907 USA

[2] Birck Nanotechnology Center, Purdue University, West Lafayette, IN 47907 USA

[3] Center for Advanced Materials, Department of Electrical and Computer Engineering, University of Houston, Houston, TX 77204 USA

[4] School of Physics, Georgia Institute of Technology, Atlanta, GA 30332 USA

[5] School of Electrical and Computer Engineering, Purdue University, West Lafayette, IN 47907 USA

# Equally contributing authors.

* Emails: qyu2@uh.edu, yongchen@purdue.edu

Abstract

We report wafer-scale graphene synthesized by chemical vapor deposition (CVD) on copper foils at ambient pressure. Graphene films up to 4 inches in size are synthesized and transferred to SiO_2/Si. Spectroscopic Raman mapping demonstrates that the synthesized films consist primarily of monolayer graphene (with as high as ~90% area coverage). Low temperature transport measurements are performed on devices made from such CVD graphene. We observe ambipolar field effect (with on/off ratio ~5 and carrier mobilities up to ~3000 cm^2/Vs) and the hall-mark "half-integer" quantum Hall effect. We also observe weak localization of carriers and extract phase coherence length up to 0.3 μm.

Graphene[1,2], a single atomic layer of graphite, is the building block of all sp^2 bonded carbon materials including graphite and carbon nanotubes. The explosion of recent interests in graphene is in a large part due to its exceptional electronic properties[3] demonstrated experimentally, such as high carrier mobility and ambipolar field effect[4], "anomalous" quantum Hall effect of massless chiral Dirac fermions[5,6], tunable electronic structure[7,8] and so on. With its potential to be used in many novel and high performance nanoelectronic devices, graphene has emerged as one of the most promising materials for "post-silicon" electronics. While the first electrically isolated graphene was fabricated by mechanical exfoliation of graphite[4], a large amount of recent efforts has been devoted to develop methods to synthesize graphene at large scale for practical electronic applications. A variety of methods, such as epitaxial growth on SiC[9,10], chemical vapor deposition (CVD) on metals[11-15], and numerous solution-based chemical approaches[16-19] have been explored. One of the most important and challenging goals is to grow graphene at large scale with uniform thickness[10,15].

Recently, large scale graphene films with excellent uniformity have been grown on Cu by CVD conducted at moderately low pressure[15]. Promising electronic properties such as ambipolar field effect with high mobilities have been demonstrated in graphene films synthesized by such a method and transferred to insulators[15]. Although it has been known for a long time that graphene can be synthesized by CVD or related surface segregation on various metals and metal carbides[18], graphene growth on Cu has only been explored quite recently[15,21,22]. One of the most commonly used metal substrates for CVD-based graphene growth has been Ni, which is capable of giving large, but generally non-uniform few-layer-graphene films[11-14, 23]. Compared to Ni, the much lower solubility of carbon in Cu[15,21,22] is believed to be key to growing graphene with uniform thickness. Studies[21] have also suggested that the growth mechanisms of graphene on Cu can be very different from that on Ni.

In this letter, we demonstrate wafer-scale growth of graphene on Cu by CVD conducted at *ambient* pressure. The synthesized films can be transferred to other substrates, such as insulating SiO_2 (on Si). We demonstrate a 4-inch graphene film, the largest reported so far to the best of our knowledge. We have performed spectroscopic Raman mapping and shown that our synthesized films consist mostly of monolayer graphene and have excellent thickness uniformity and crystalline quality. The electronic properties of the transferred CVD-grown graphene are studied by variable temperature electrical/magneto-transport measurements. In addition to ambipolar field effect with high mobilities, we observe half-integer quantum Hall effect (QHE), a hall-mark of the unique electronic properties of monolayer graphene. We also study the weak localization, from which we extract information on carrier scattering and phase coherence. Our results will be important for understanding the properties of CVD-

grown graphene on Cu and using such large scale graphene in fundamental research or electronic applications.

Except for the different CVD growth pressure, our recipe for graphene synthesis (conducted at ambient pressure) is largely similar to that in Ref. 15 (which uses low pressure). Briefly, polycrystalline Cu foils with thickness of 25 μm and purity >99.8% from Alfa Aesar are used as growth substrates. The precursor gas used is CH_4 (70 ppm) carried by H_2:Ar (1:30), with a total gas flow rate of 310 sccm at the pressure of 1 atm. The growth temperature is set at 1000 ˚C (10 min) for the decomposition of CH_4 (catalyzed[24] by Cu), leading to carbon deposition and graphene formation. The samples are then cooled down by mechanically pushing the sample holder through lower temperature zones to room temperature in Ar atmosphere. The cooling rate (~10 ˚C/s, an average value cooling from 1000 to 700 ˚C) is measured by a thermocouple attached to the sample holder. Fig. 1a shows a 4 in × 4 in Cu foil taken out from the CVD chamber. The highly transparent CVD graphene covering the Cu is hardly visible.

We have transferred the graphene grown on Cu to other substrates (such as glass, Si wafer covered with SiO_2, or plastics) using PMMA (polymethyl methacrylate), similar to the processes described in Ref. 15. The as-synthesized samples are spin-coated by PMMA, with the spinning speed ranging between 500 to 3000 rpm depending on the size of sample. A slow spinning speed (giving rise to relatively thick PMMA film) is found to be preferable for transferring large sized graphene, e.g. the 4 in × 4 in film in Fig. 1. After coating PMMA, the sample is placed in an aqueous solution of iron nitrate to etch off the Cu substrate (Fig.1b, showing a 4-in graphene film covered with PMMA floating on the surface of solution). Afterwards, the graphene with PMMA coating is scooped out from the solution by the transfer substrate. The PMMA is then removed by acetone and the sample is rinsed several times by de-ionized water. Fig. 1c shows the 4-in graphene transferred on a large Si wafer. For all the data presented below, the transfer substrates used are highly doped Si wafer covered by 300nm-thick thermally grown SiO_2 and are simply referred to as SiO_2/Si.

Raman spectroscopy is a powerful, yet relatively simple method to characterize the thickness and crystalline quality of graphene layers[12,13,15,25-27]. We have performed Raman spectroscopy (excitation laser wavelength = 532nm) and Raman mapping on the CVD graphene films transferred to SiO_2/Si. In particular, we have used such spatially resolved Raman measurements to probe the uniformity of our large-scale CVD graphene. Fig. 2a shows a representative Raman map showing the intensity ratio of 2D and G bands (I_{2D}/I_G) measured in a 10 μm ×10 μm area of a CVD graphene sample (the corresponding optical microscope image of the scanned area is shown as the inset of Fig. 2b). Details of our data

analysis, including the precise definition of various Raman spectral bands (labeled in Fig.2b) and the procedure used to extract their intensity, and the mapping of individual bands, are given in the Supporting Information (SI). We find that ~99% of the area mapped show $I_{2D}/I_G > 2$, ~93% of the area mapped show $I_{2D}/I_G > 3$ and about half of the area show $I_{2D}/I_G > 4$ (the medium value, see SI). It is known that I_{2D}/I_G is dependent on the number of graphene layers[12,13,15,25-27]. For example, our measurements (under similar experimental conditions as we used in Fig. 2) on exfoliated graphene layers give typical I_{2D}/I_G ~2-3 for monolayer samples and I_{2D}/I_G slightly lower than 1 for bilayers. Previous studies[15] of CVD-grown graphene (transferred from Cu) have taken a I_{2D}/I_G ~2 to indicate monolayer graphene, $2 > I_{2D}/I_G > 1$ for bilayer and $I_{2D}/I_G < 1$ for multilayers. The position and/or line-shape of the 2D band is also a sensitive probe of the thickness of exfoliated graphene layers[25-27], but not necessarily so for CVD-grown ones due to possible stacking disorder[12]. Based on our I_{2D}/I_G data, we conclude that most of the area mapped is monolayer graphene. We also notice that, even in locations with $I_{2D}/I_G > 2$, believed to indicate monolayer, we can still observe substantial variation in I_{2D}/I_G (as seen, for example, in several Raman spectra in Fig. 2b measured from the corresponding marked spots in Fig.2a). We speculate that one possible reason for this variation and sometimes very large I_{2D}/I_G (e.g. >5) may be the spatially non-uniform adhesion (bonding) between the transferred graphene film and the underlying substrate (SiO_2), as it has been shown that the supporting substrate can strongly affect the Raman spectrum for monolayer graphene (the influence is weaker for bilayers)[28]. The disorder-induced D band in the spectra shown in Fig.2b is seen to be very small, indicating high crystalline quality of the graphene[15,25-27]. Fig. 2c shows the Raman map of I_D/I_G of the same area scanned in Fig. 2a. The mean value of I_D/I_G is less than 0.1 (see SI, Fig. S1b). Lower-spatial-resolution mapping over larger areas have shown qualitatively similar results as described above. For example, Fig. 2d shows a 200 μm ×200 μm Raman map of I_{2D}/I_G, with ~99% of the area having $I_{2D}/I_G > 2$ and ~90% of the area having $I_{2D}/I_G > 3$ and ~41% of the area having $I_{2D}/I_G > 4$. We have also obtained qualitatively similar Raman maps from many smaller (~10 μm, similar to Fig. 2a) areas randomly selected from different locations of a large-scale CVD graphene film. Several of these areas have been subsequently fabricated into devices and an independent and more unambiguous verification of monolayer graphene has been performed using quantum Hall measurements (presented in Fig.3). Our results suggest that our CVD graphene films have excellent quality and uniformity, consisting mainly of monolayer.

To study the electronic properties of the transferred graphene, we have fabricated them into quasi-Hall-bar-shaped devices using standard e-beam lithography or photolithography, O_2 plasma etching and metallization (with evaporated Ti/Au contact electrodes). The optical image of a representative device ("A") is shown in the inset of Fig. 3a. We have measured several such devices and found similar results

(including the quantum Hall effects). The data from two devices ("A" and "B") are presented below. In our experiments the electrical resistances are measured by low frequency lock-in detection with a low driving current (10 nA). The carrier density in the device can be tuned by a back gate voltage (V_{gate}) applied to the highly doped Si substrate, with the 300nm thermally grown SiO_2 as the gate dielectric.

Fig. 3a shows four terminal resistance (R_{xx}) as a function of V_{gate} measured in device "A" at low temperature (T=0.6 K) and zero magnetic field. The data display the characteristic "ambipolar" field effect[4-6,12,13,15,23], where the resistance can be modulated by a factor of more than 5. The charge neutral "Dirac point" (DP) can be determined from the position (V_{DP}~20V for this sample) of the peak in resistance (the positive V_{DP} indicates the sample has some "residual" hole-doping, which is extrinsic in origin and common in fabricated graphene devices[4]). The field effect mobility has been extracted to be ~3000 cm^2/Vs for holes (p-type, $V_{gate}<V_{DP}$) and ~1000 cm^2/Vs for electrons (n-type, $V_{gate}>V_{DP}$), at sufficiently large $|V_{gate} - V_{DP}|$ (corresponding to carrier density on the order of ~$10^{12}/cm^2$). Similar field effect is also observed at room temperature, although we can access a larger range of V_{gate} at lower temperatures without gate leakage.

Fig.3b shows R_{xx} (4-terminal longitudinal resistance) and R_{xy} (Hall resistance) of device "A" as a function of V_{gate} measured at a high magnetic field (B=18T, applied perpendicular to the sample) and low temperature (T=0.7 K). The sign reversal of R_{xy} from $V_{gate}>V_{DP}$ to $V_{gate}<V_{DP}$ is consistent with the ambipolar field effect (change of carrier types). Most remarkably, R_{xy} is seen to exhibit clearly quantized plateaus at $h/(2e^2)$ for electrons, $-h/(2e^2)$, $-h/(6e^2)$ and $-h/(10e^2)$ for holes, all accompanied by vanishing R_{xx}, where e is the elementary charge and h is the Plank constant. This is the so-called "half-integer" quantum Hall effect (QHE), an electronic hall-mark of monolayer graphene[5,6], with vanishing R_{xx} and quantized Hall (R_{xy}) plateaus corresponding to $R_{xy}^{-1}=\pm 4(N+1/2)e^2/h$ (where N is a non-negative integer, and the plus/minus sign indicates the carrier type being electrons/holes), occurring at the Landau Level (LL) filling factor $\nu=nh/eB=4(N+1/2)$ (where n is the 2D carrier density). The LL filling factor ν for the observed quantum Hall (QH) states in Fig. 3b is indicated near the corresponding Hall plateaus. We have also measured R_{xx} (magnetoresistance) and R_{xy} (Hall effect) as functions of the magnetic field (B) at fixed V_{gate}. The "Hall" mobilities extracted from such measurements are found to be comparable with the "FET" mobilities extracted from the field effect (Fig. 3a) described earlier.

Fig. 3c shows R_{xx} and R_{xy} measured between B=0T and 18T at V_{gate}=75V (electrons), and Fig. 3d shows similar measurements at V_{gate}=0V (holes, with opposite sign of R_{xy} from that of electrons). The ν=2 QH state is well resolved in both cases. A developing QH state for ν=10 is also observed in Fig. 3d. We note

that the half integer QHE was first observed in exfoliated graphene[5,6] and has been observed only very recently in various synthesized graphene, including epitaxial graphene grown on SiC[29-32],CVD graphene grown on Ni[13], and now CVD graphene grown on Cu. Observation of the QHE is an important indication that the graphene fabricated by these synthetic (and more scalable) approaches possesses the intrinsic graphene properties with electronic quality approaching or comparable with graphene exfoliated from graphite.

In addition to QHE at relatively high *B*, we have also studied the temperature-dependent low-*B* magnetoresistance to probe carrier coherence and scattering. Fig. 4a shows $\Delta R_{xx}(B)= R_{xx}(B)-R_{xx}(B=0T)$ measured at various temperatures (T) in device "B". The low *T* (e.g., 1.5 K) magnetoresistance displays two pronounced features, which weakens (and eventually disappears) at elevated *T*: 1) reproducible fluctuations, which we associate as the universal conductance fluctuation (UCF)[33]; 2) an overall *negative* (except for fluctuations) magnetoresistance for B<~0.5T (with a resistance peak at 0T), which we interpret as due to weak localization (WL)[33-35]. Both UCF and WL are mesoscopic quantum transport phenomena related to phase coherence of charge carriers. Below we present a more detailed discussion of WL, which has been studied in a variety of graphene and graphitic thin films fabricated by different methods[23, 36-43] and can yield a wealth of information about the carrier transport (esp. various scattering processes) and disorder in the sample.

WL[33-35] arises from the constructive interference between time-reversed multiple-scattering trajectories (within a length-scale L_φ that the carrier wave function is phase coherent). Such a constructive interference leads to coherent backscattering of carriers and enhance the electrical resistance. The low *T* negative magnetoresistance is understood because the WL can be destroyed by either raising *T*, which destroys the constructive interference, or applying a perpendicular *B*, which breaks the time-reversal symmetry. Being a quantum coherent process, WL in general is sensitive to inelastic scattering (phase-breaking) processes of charge carriers[33-35]. Due to the chiral nature of carriers, WL in graphene is also sensitive to various elastic scattering processes[38, 39, 44]. For a more quantitative analysis, we have fitted (Fig. 4b inset) our experimental data by the WL theory developed for mono-layer graphene[44]:

$$\Delta\sigma_{xx}(B) = \left(\frac{e^2}{\pi h}\right)\left(F[\frac{B}{B_\varphi}] - F[\frac{B}{B_\varphi + 2B_i}] - 2F[\frac{B}{B_\varphi + B_i + B_*}] \right) \quad (1)$$

$F(z) = \ln z + \psi\left(\frac{1}{2}+\frac{1}{z}\right)$, and $B_{\varphi,i,*} = (h/8\pi e)L^{-2}_{\varphi,i,*}$.

Here, $\Delta\sigma_{xx}(B)= \sigma_{xx}(B)-\sigma_{xx}(B=0T)$. The conductivity is defined as $\sigma_{xx}=L/(W\times R_{xx})$, where W and L are the width and length of the sample, respectively. Ψ in (1) is the digamma function. L_φ is the aforementioned phase coherence length, associated with inelastic scattering processes responsible for the dephasing of charge carriers. L_i and L_* are intervalley and intravalley scattering lengths respectively, both due to elastic scattering processes. Fig. 4b shows L_φ , L_i and L_* thus extracted and plotted as functions of T. L_φ increases with decreasing T, reaching ~0.3 μm at T=1.5 K. We have independently extracted L_φ by analyzing the UCF as a function of B[9, 37, 45, 46] and found the values to be comparable with those obtained from the WL analysis. The reduced L_φ at elevated T would lead to the destruction of quantum interference that underlies WL, explaining the T-dependence of the magnetoresistance. This is also consistent with our finding that $R_{xx}(B=0T)$ decreases with increasing T (up to ~80K reached in this measurement). Different from L_φ, the values of L_i and L_* are found to be relatively temperature-insensitive. The fact that all these scattering lengths (L_φ, L_i and L_*) are much smaller than the sample size (~3 μm) suggests that the dominant scattering source is not the edge, but rather disorder within the sample, such as impurities trapped near graphene or various defects in the graphene lattice structure[3,38,39,44]. It has been pointed out that inter-valley scattering is essential for WL in graphene, and such scattering processes require atomically-sharp disorder (e.g., point defects)[38,39,44]. Our observation of a relatively short L_i (<~150 nm) indicates that an appreciable amount of such disorder is present in our sample. Moreover, the observation of even shorter L_* ($<L_i$) suggests the presence of additional source of disorder, such as lattice defects larger than atomic scale (e.g. line defects, dislocations, ripples etc)[38]. One interesting question worth further investigations (for example, using a series of samples prepared under different conditions) is how the weak localization data (suggesting various possible defects discussed above) may correlate with the Raman data (e.g. small but finite "D" bands occasionally observed). An in-depth understanding of the disorder will be important for the electronic applications as well as understanding the growth and defect formation mechanisms of such graphene films.

In summary, we have demonstrated wafer-scale graphene with dominant monolayer coverage grown by ambient pressure CVD on Cu. Our transferrable CVD graphene show intrinsic graphene behavior such as half-integer quantum Hall effect, and other excellent electronic properties characterized by the ambipolar field effect, carrier mobility and phase coherence. The large, flexible and transferrable graphene films synthesized with a scalable and simple method and possessing excellent uniformity and quality as demonstrated in this work can enable a wide range of practical applications exploiting the exceptional properties of graphene.

Acknowledgements. Acknowledgment is made to Miller Family Endowment, Midwest Institute for Nanoelectronics Discovery (MIND), Indiana Economic Development Corporation (IEDC), American Chemical Society and CAM Special Funding for partial support of this research. A portion of the low temperature magnetotransport measurements was carried out at the National High Magnetic Field Laboratory, which is supported by NSF Cooperative Agreement No. DMR-0084173, by the State of Florida and DOE. We thank Glover Jones, Tim Murphy, Jun-Hyun Park and Eric Palm for experimental assistance. We also thank Robert Colby, Deepak Pandey and Eric Stach for helpful discussions.

REFERENCES

1. Geim, A.K. *Science* **2009**, *324*, 1530.

2. Geim, A.K.; Novoselov, K.S. *Nature Mat.* **2007**, *6*, 183.

3. Castro Neto, A. H.; Guinea, F.; Peres, N. M.; Novoselov, K. S.; Geim, A. K. Rev. Mod. Phys. **2009**, *81*, 109.

4. Novoselov, K. S.; Geim, A. K.; Morozov, S. V.; Jiang, D.; Zhang, Y.; Dubonos, S. V.; Grigorieva, I. V.; Firsov, A. A. *Science* **2004**, *306*, 666.

5. Novoselov, K. S.; Geim, A. K.; Morozov, S. V.; Jiang, D.; Katsnelson, M. I.; Grigorieva, I. V.; Dubonos, S. V.; Firsov, A. A. *Nature* **2005**, *438*, 197.

6. Zhang, Y.; Tan, Y. W.; Stormer, H. L.; Kim, P. *Nature* **2005**, *438*, 201.

7. Han, M.Y.; Oezyilmaz, B.; Zhang, Y.; Kim, P. *Phys. Rev. Lett*, **2007**, *98*, 206805.

8. Chen, Z.; Lin, Y.; Rooks, M.J.; Avouris, P. *Physica E* **2007**, *40*, 228.

9. Berger, C.; Song, Z.; Li, X.; Wu, X.; Brown, N.; Naud, C.; Mayou, D.; Li, T.; Hass, J.; Marchenkov, A. N.; Conrad, E. H.; First, P. N.; de Heer, W. A. *Science* **2006**, *312*, 1191.

10. Emtsev, K. V.; Bostwick, A.; Horn, K.; Jobst, J.; Kellogg, G. L.; Ley, L.; McChesney, J. L.; Ohta, T.; Reshanov, S. A.; Röhrl, J.; Rotenberg, E.; Schmid, A. K.; Waldmann, D.; Weber, H. B.; Seyller, T. *Nature Mater*. **2009**, 8, 203.

11. Yu, Q. K.; Lian. J., Siripongert, S.; Li, H.; Chen, Y. P.; Pei. S. S. *Appl. Phys. Lett.* **2008**, *93*, 113103.

12. Reina, A.; Jia, X.; Ho, J.; Nezich, D.; Son, H.; Bulovic, V.; Dresselhaus, M. S.; Kong, J. *Nano Lett.* **2009**, *9*, 30.

13. Kim, K. S.; Zhao, Y.; Jang, H.; Lee, S. Y.; Kim, J. M.; Kim, K. S.; Ahn, J. H.; Kim, P.; Choi, J. Y.; Hong, B. H. *Nature* **2009**, *457*, 706.

14. Gomez De Arco, L.; Zhang, Y.; Kumar, A.; Zhou, C. *IEEE Trans. Nanotech*. **2009**, *8*, 135.

15. Li, X.; Cai, W.; An, J.; Kim, S.; Nah, J.; Yang, D.; Piner, R.; Velamakanni, A.; Jung, I.; Tutuc, E.; Banerjee, S. K.; Colombo, L.; Ruoff, R. S. *Science* **2009**, *324*, 1312.

16. Park, S.; Ruoff, R. S. *Nature Nanotech.* **2009**, *4*, 217.

17. Gilje, S.; Han, S.; Wang, M.; Wang, K. L.; Kaner R.B. *Nano Lett*. **2007**, *7*, 3394.

18. Gomez-Navarro, C.; Weitz, R. T.; Bittner, A. M.; Scolari, M.; Mews, A.;Burghard, M.; Kern, K.; *Nano Lett*. **2007**, *7*, 3499.

19. Cote, L.J.; Kim, F.; Huang, J. *J. Am. Chem. Soc.* **2009**, *131*, 1043.

20. Oshima, C.; Nagashima, A. *J. Phys. Cond. Mat.* **1997**, *9*, 1.

21. Li, X.; Cai, W.; Colombo, L.; Ruoff, R. S. *Nano Lett.* **2009**, ASAP **DOI:** 10.1021/nl902515k.

22. Yu, Q.; Lian, J.; Siriponglert, S.; Li, H.; Chen, Y. P.; Pei, S.S. arXiv:0804.1778v1, **2008**.

23. Cao, H.; Yu, Q. K.; Pandey, D.; Zemlianov, D.; Colby, R.; Childres, I.; Drachev, V.; Stach, E.; Lian, J.; Li, H.; Pei, S. S.; Chen, Y. P. arXiv:0901.1136v2, **2009**.

24. Zhou, W. W.; Han, Z. Y.; Wang, J. Y.; Zhang, Y.; Jin, Z.; Sun, X.; Zhang, Y. W.; Yan, C. H.; Li, Y. *Nano Lett.* **2006**, 6, 2987.

25. Ferrari, A. C.; Meyer, J. C.; Scardaci, V.; Casiraghi, C.; Lazzeri, M.; Mauri, F.; Piscanec, S.; Jiang, D.; Novoselov, K. S.; Roth, S.; Geim, A. K. *Phys. Rev. Lett.* **2006**, *97*, 187401.

26. Gupta, A.; Chen, G.; Joshi, P.; Tadigadapa, S.; Eklund, P. C. *Nano Lett.*, **2006**, *6*, 2667.

27. Graf, D.; Molitor, F.; Ensslin, K.; Stampfer, C.; Jungen, A.; Hierold, C.; Wirtz, L. *Nano Lett.*, **2007**, *7*, 238.

28. Berciaud, S.; Ryu, S.; Brus, L.E.; Heinz, T.F. *Nano Lett.*, **2009**, *9*, 346.

29. Jobst, J.; Waldmann, D.; Speck, F.; Hirner, R.; Maude, D. K.; Seyller, T.; Weber, H. B. arXiv:0908.1900v1 **2009**.

30. Shen, T.; Gu, J. J.; Xu, M.; Wu, Y. Q.; Bolen, M. L.; Capano, M. A.; Engel, L. W.; Ye, P. D. arXiv:0908.3822v2 **2009**.

31. Wu, X.; Hu, Y.; Ruan, M.; Madiomanana, N. K.; Hankinson, J.; Sprinkle, M.; Berger, C.; de Heer, W. A. arXiv:0909.2903v1 **2009**.

32. Lara-Avila, S.; Kalaboukhov, A.; Paolillo, S.; Syväjärvi, M.; Yakimova, R.; Fal'ko, V.; Tzalenchuk, A.; Kubatkin, S. arXiv:0909.1193 **2009**.

33. Beenakker, W. J.; van Houten, H. *Quantum Transport in Semiconductor Nanostructures*, vol. 44 (Academic Press, New York, **1991**), and reference therein (also available at arxiv.org/abs/cond-mat/0412664).

34. Lin, J. J.; Bird, J. P. *J. Phys.: Condens. Matter* **2002**, *14*, R501.

35. Bergmann, G. *Phys. Rep*. **1984**, *107*, 1.

36. Koike, Y.; Morita, S.; Nakanomyo, T.; Fukase, T. *J. Phys. Soc. Jpn.* **1985**, *54*, 713.

37. Morozov, S. V.; Novoselov, K. S.; Katsnelson, M. I.; Schedin, F.; Ponomarenko, L. A.; Jiang, D.; Geim, A. K. *Phys. Rev. Lett*. **2006**, *97*, 016801.

38. Tikhonenko, F. V.; Horsell, D. W.; Gorbachev, R. V.; Savchenko, A. K. *Phys. Rev. Lett.* **2008**, *100*, 056802.

39. Ki, D.; Jeong, D.; Choi, J.; Lee. H.; Park, K. *Phys. Rev. B* **2008**, *78*, 125409.

40. Gorbachev, R. V.; Tikhonenko, F. V.; Mayorov, A. S.; Horsell, D. W.; Savchenko, A. K. *Phys. Rev. Lett.* **2007**, *98*, 176805.

41. de Heer, W. A; Berger, C.; Wu, X.; First, P. N.; Conrad, E. H.; Li, X.; Li, T.; Sprinkle, M.; Hass, J.; Sadowski, M. L.; Potemski, M.; Martinez, G. *Solid State Commun.* **2007**, *143*, 92.

42. Wu, X.; Li, X.; Song, Z.; Berger, C.; de Heer, W. A. *Phys. Rev. Lett.* **2007**, *98*. 136801.

43. Shen, T.; Wu, Y. Q.; Capano, M. A.; Rokhinson, L. P.; Engel, L. W.; Ye, P. D. *Appl. Phys. Lett.* **2008**, *93*, 122102.

44. McCann, E.; Kechedzhi, K.; Fal'ko,V. I.; Suzuura, H.; Ando, T.; Altshuler, B. L. *Phys. Rev. Lett.* **2006**, *97*, 146805.

45. Weng, L.; Zhang, L.; Chen, Y. P.; Rokhinson, L. P. *Appl. Phys. Lett.* **2008**, *93*, 093107.

46. Staley, N. E.; Puls, C. P.; Liu, Y. *Phys. Rev. B* **2008**, *77*, 155429.

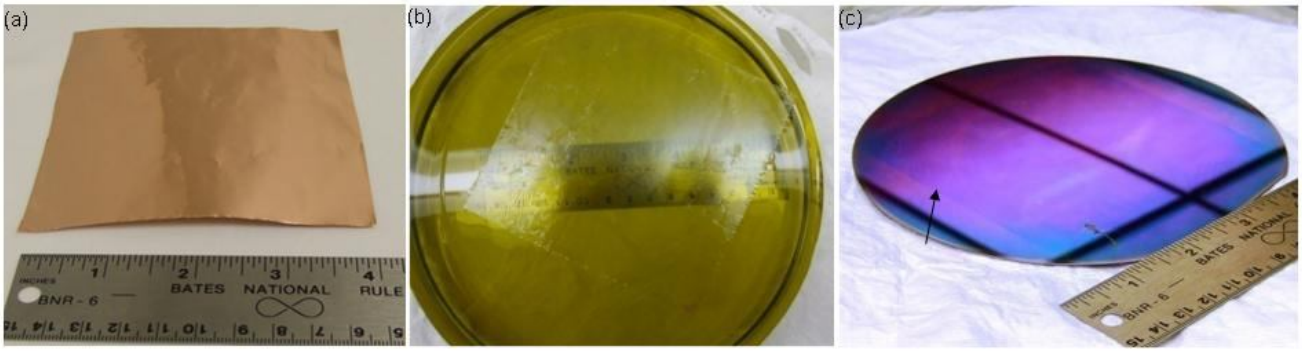

Fig.1. Photographs of large scale CVD graphene grown on Cu. (a) A 4 in x 4 in Cu foil used as the substrate for CVD graphene growth. (b) A 4 in x 4 in CVD graphene film coated with PMMA and floating on liquid. (c) The graphene film in (b) transferred on a large Si wafer, after removing the PMMA. The arrow marks the edge of the graphene film. The film has a slightly different color contrast from the wafer. The image with thick black lines on the wafer is reflection of the clean room ceiling.

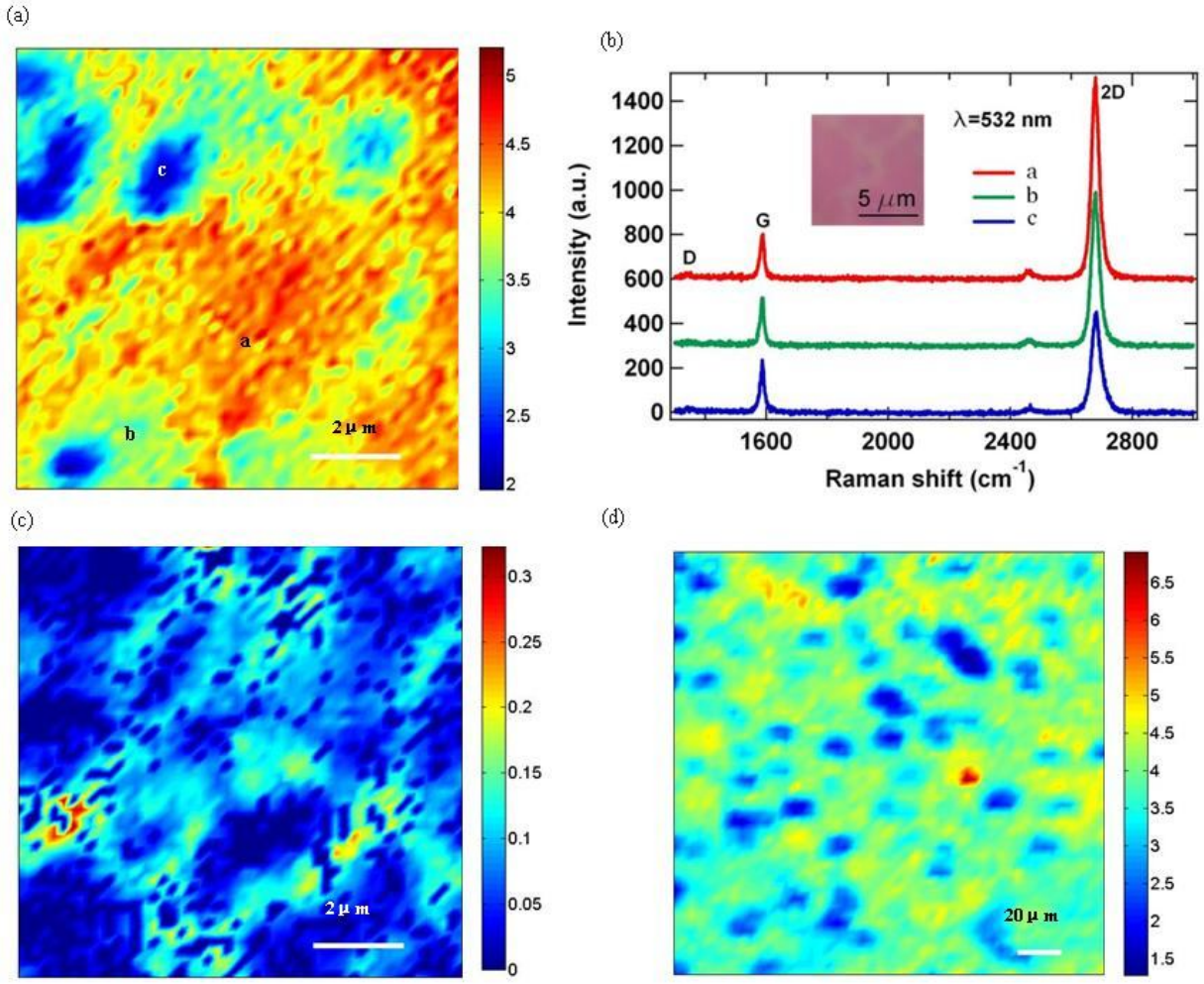

Fig.2. Raman spectroscopy and mapping of the CVD graphene transferred to SiO_2/Si. The wavelength of the excitation laser is 532 nm. (a) Raman map of the intensity ratio (I_{2D}/I_G) of 2D band to G band measured in an area of 10 μm ×10 μm. The size of the scanning step (defining the pixel size) is 0.2μm. Most area can be associated with monolayer (I_{2D}/I_G >2, see text). (b) Raman spectra (offset for clarity) measured from the marked spots in (a). The D, G, and 2D bands are labeled in the spectra. The 2D band of each spectrum can be fitted by a single Lorentzian, with center at ~2680 cm^{-1} and FWHM (full width at half maximum) ~34 cm^{-1}, consistent with the values previously observed for similar CVD graphene[15]. The inset shows the optical image of the area mapped in (a). (c) Raman map of the "D/G" intensity ratio (I_D/I_G) obtained from the same area as in (a). I_D/I_G is related to the amount of defects in the graphene. (d) Raman map of I_{2D}/I_G measured from a larger area (200 μm × 200 μm, with 5μm pixel size). The objective lens used in (a-c) is 100×, and that in (d) is 20×. Details of data analysis can be found in the Supporting Information (SI).

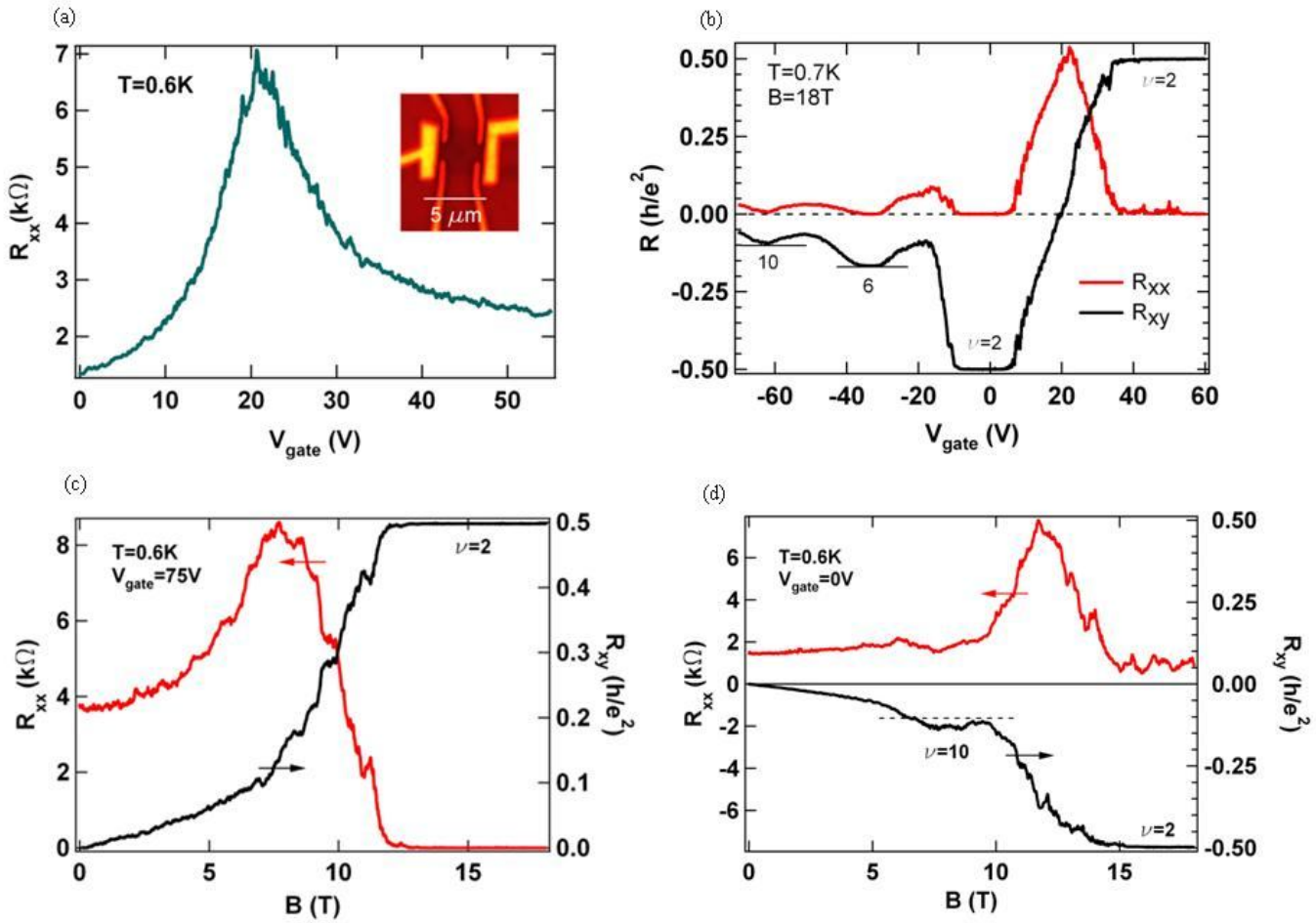

Fig. 3. Ambipolar field effect and half integer quantum Hall effect (QHE) of CVD graphene. (a) Four-terminal longitudinal resistance (R_{xx}) as a function of gate voltage (V_{gate}) measured in device "A" (optical microscope image shown in the inset). (b) R_{xx} and R_{xy} (Hall resistance) as a function of gate voltage at perpendicular magnetic field B=18T and low temperature (T=0.7K). (c), (d) R_{xx} and R_{xy} as functions of B at T=0.6K for V_{gate} =75V (n-type carriers) and V_{gate} =0V (p-type carriers), respectively. The Landau filling factors (ν) of the observed half-integer quantum Hall (QH) states are labeled in (b-d) and selected QHE plateaus corresponding to R_{xy} $=h/\nu e^2$ are indicated by horizontal lines as guide to the eye.

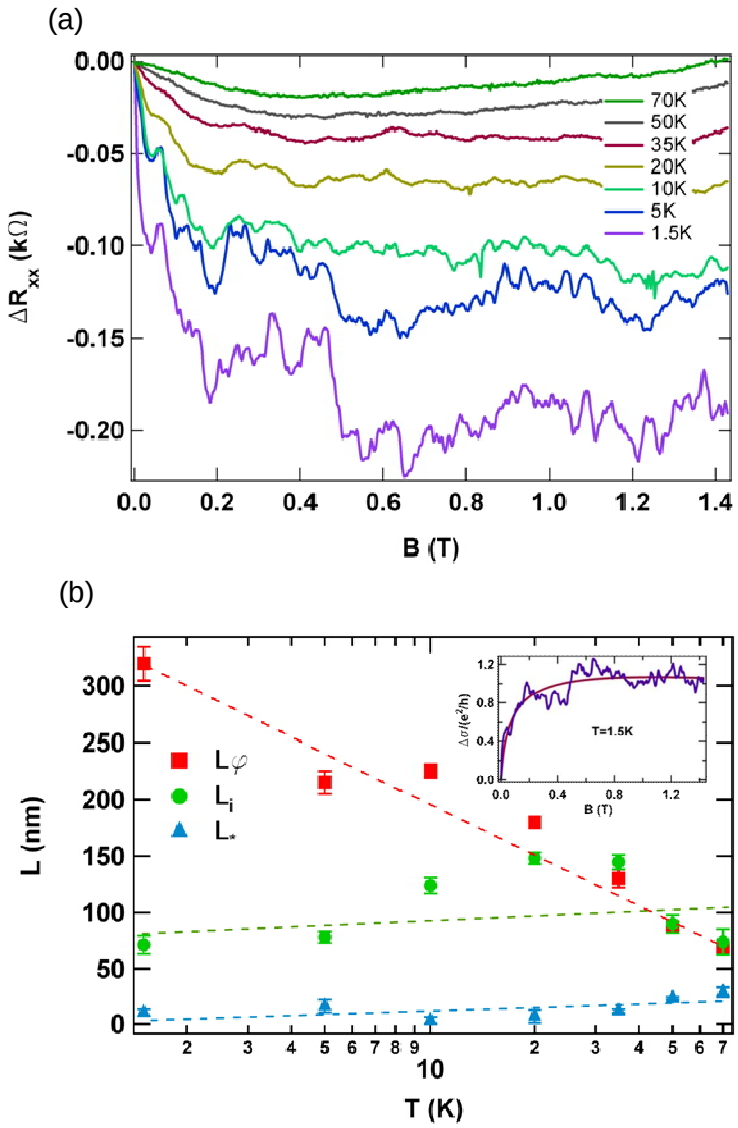

Fig. 4. Temperature dependent magneto-transport and weak localization. (a) Magnetoresistance $\Delta R_{xx}(B) = R_{xx}(B) - R_{xx}(B=0T)$ measured in device "B" at various temperatures. (b) Extracted characteristic lengths from weak localization as a function of the temperature. Dashed lines are guides to the eye. Inset shows the magnetoconductivity (normalized by e^2/h) $\Delta\sigma_{xx}(B) = \sigma_{xx}(B) - \sigma_{xx}(0T)$ at T=1.5 K. Solid line is the fit using the WL theory developed for graphene (see text).

Supporting Information

Details and Supplemental Data on Raman Spectroscopy and Raman Mapping

Our Raman measurements were performed with a Horiba LabRam confocal Raman microscope with a motorized sample stage (for Raman mapping). The wavelength of the excitation laser we used is 532nm (similar to that used in Ref. 15, X. Li *et al*., Science **324**, 1312, 2009) and we have kept the power low enough (typically on the order of 1mW at the sample) in the "linear" regime, that is, further reducing the power would not give appreciable change in the intensity ratios (defined below) between relevant Raman bands (but will give more noise in the spectra). The laser spot size is ~0.6μm and 1.3μm respectively for 100X and 20X objectives we used.

We use the following intervals for the range of the D, G, and 2D bands:

Band (x)	x_0 (start)	x_1 (end)
D	1320 cm^{-1}	1380 cm^{-1}
G	1560 cm^{-1}	1620 cm^{-1}
2D	2640 cm^{-1}	2720 cm^{-1}

To extract the intensity of a given band, I_x (where x=D, G, or 2D), we perform a best Lorentzian ($f(x)= y_0 + Aw/(w^2+4(x-x_0)^2)$) fit to the peak over the corresponding range defined above. The intensity (I_x) is defined by the amplitude value (A/w) of the Lorentzian function fit.

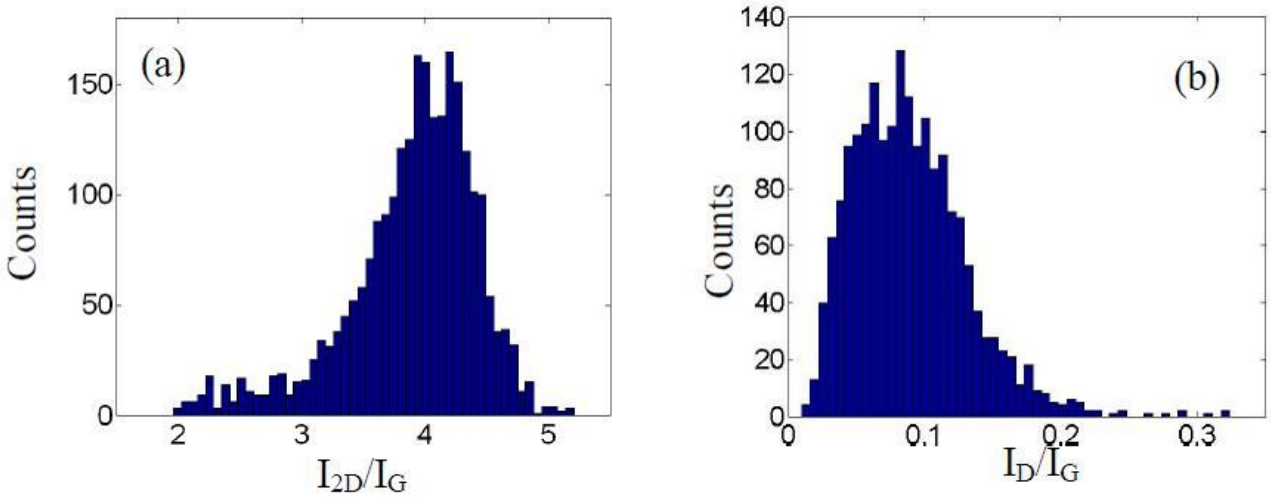

Figure S1. (a) Histogram of I_{2D}/I_G (2D/G ratio) in the Raman map shown in Fig. 2a. We find <1% of the scan area (inset of Fig. 2b) having $1< I_{2D}/I_G <2$, >99% of the area having $I_{2D}/I_G >2$ and ~93% of the area having $I_{2D}/I_G >3$. There are no spectra with $I_{2D}/I_G <1$. (b) Histogram of I_D/I_G of the Raman map shown in Fig. 2c. Only the spectra (1890 out of 2500) with an observable "D" peak (allowing a Lorentzian fit) are included in the histogram.

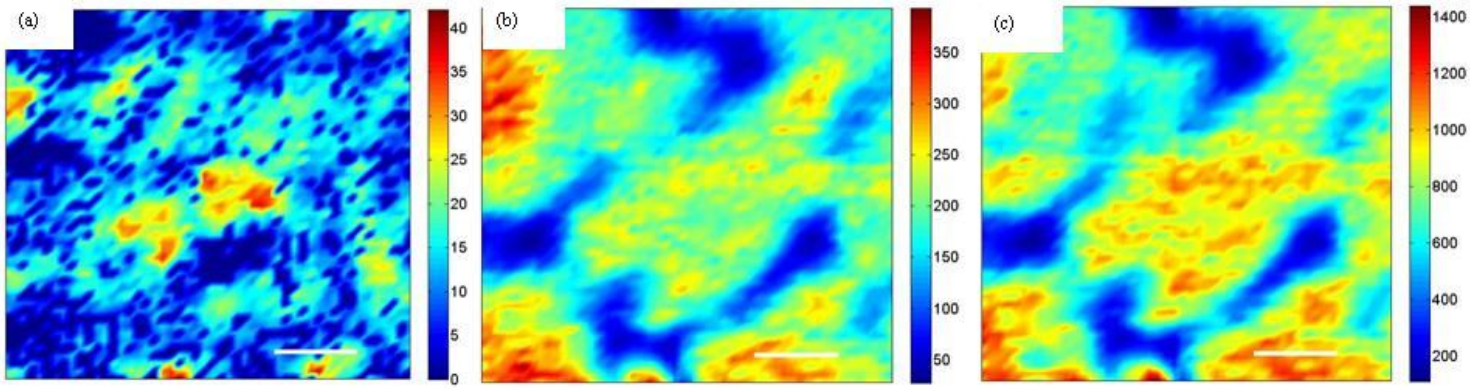

Figure S2. Raman maps for I_D (a), I_G (b), and I_{2D} (c) respectively for the same scan area as in Fig 2(a,c). The scale bar is 2μm.

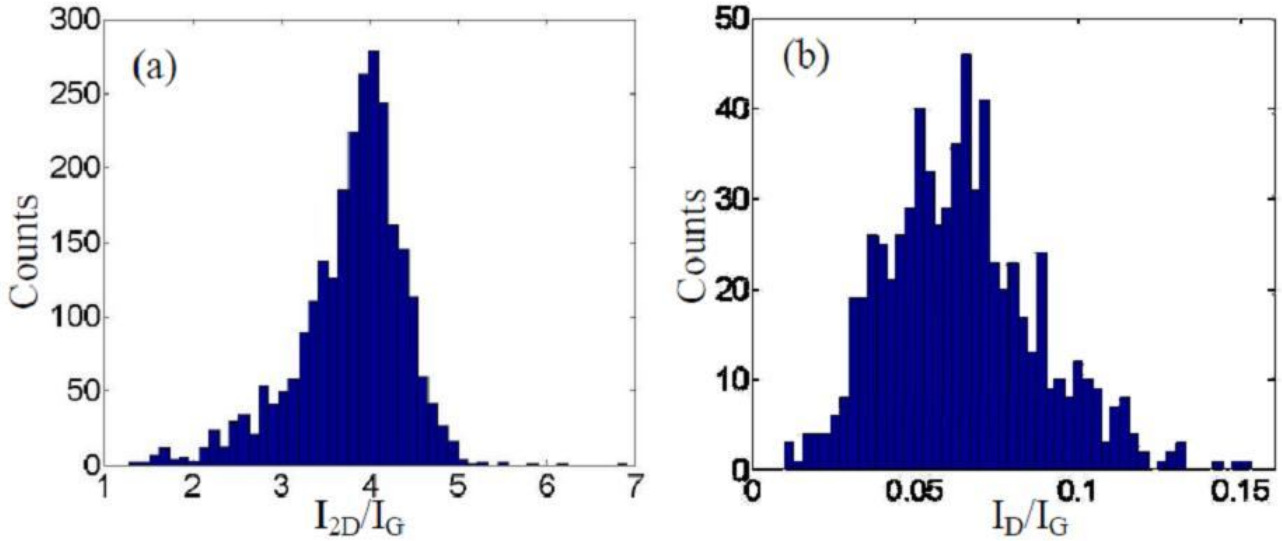

Figure S3 (a) Histogram of the I_{2D}/I_G of the large-area (200μm x 200μm) Raman map shown in Fig. 2d. We find ~1% of the area having $1< I_{2D}/I_G <2$, ~99% of the area having $I_{2D}/I_G >2$ and ~90% of the area having $I_{2D}/I_G >3$. There are no spectra with $I_{2D}/I_G <1$. (b) Histogram of the I_D/I_G of the large-area (200μm x 200μm) Raman map shown in Fig. 2d. Only 689 out of 2601 spectra have an observable "D" peak (allowing a Lorentzian fit) and are included in the histogram.